This is a preprint, the final version is subject to change, of the American Mineralogist (MSA)
Cite as Authors (Year) Title. American Mineralogist, in press.
DOI: https://doi.org/10.2138/am-2020-7228

Imaging trace element zoning in pyroxenes using synchrotron XRF mapping with the Maia detector array: benefit of low incident energy

Stephen J. Barnes[1], David Paterson[2], Teresa Ubide[3], Louise E. Schoneveld[1], Chris Ryan[4], Margaux Le Vaillant[1]

[1]CSIRO Mineral Resources, Kensington, Australia; [2]Australian Synchrotron, ANSTO, Clayton, Aus; [3]School of Earth and Environmental Sciences, The University of Queensland, Brisbane, Aus; [4]CSIRO Mineral Resources, Clayton, Aus.

Revision 1

Abstract

Trace element zoning in igneous phenocrysts and cumulus phases is an informative record of magmatic evolution. The advent of microbeam X-ray fluorescence (XRF) mapping has allowed rapid chemical imaging of samples at thin section to decimetre scale, revealing such zoning patterns. Mapping with synchrotron radiation using multidetector arrays has proved especially effective, allowing entire thin sections to be imaged at micron scale resolution in a matter of hours. The resolution of subtle minor element zoning, particularly in first row transition metals, is greatly enhanced in synchrotron X-ray fluorescence microscopy (XFM) images by scanning with input beam energy below the Fe Kα line. In the examples shown here, from a phenocryst rich trachybasalt from Mt Etna (Italy) and from a Ni-Cu-PGE ore-bearing intrusion at Norilsk (Siberia), the zoning patterns revealed in this way record aspects of the crystallisation history that are not readily evident from XFM images collected using higher incident energies and that cannot be obtained at comparable spatial resolutions by any other methods within reasonable scan times. This approach has considerable potential as a geochemical tool for investigating magmatic processes and is also likely to be applicable in a wide variety of other fields.

Introduction

Trace element zoning patterns in igneous phenocrysts and cumulus minerals are useful recorders of magmatic histories within subvolcanic plumbing systems (Ubide and Kamber, 2018). They have been used as evidence for supercooling (Mollo et al., 2013), multi-stage cooling histories (Ubide et al., 2019), crystal residence times in magmatic reservoirs (Costa and Morgan, 2011) and assimilation of country rocks in magmatic sulfide hosting intrusive systems (Barnes et al., 2016a; Mao et al., 2019). These patterns have been imaged by a variety of different techniques including laser ablation – inductively coupled plasma mass spectrometry (LA-ICPMS) mapping (Lynn et al., 2018; Ubide and Kamber, 2018; Ubide et al., 2015, 2019), time-of-flight LA-ICP-TOFMS mapping (Ubide et al.,

2019b), wavelength dispersive electron microprobe mapping (Welsch et al., 2013), Nano-scale Secondary Ion Mass Spectrometry (Nano-SIMS) (Seitz et al., 2018) and various techniques of microbeam X-ray fluorescence microscopy (XFM) (Barnes et al., 2016a; Barnes et al., 2016b; Barnes et al., 2018; Mao et al., 2019; Wang et al., 2019). The latter technique has been enhanced by the advent of the Maia multidetector array coupled with synchrotron microbeam sources (Paterson et al., 2011; Ryan et al., 2014a; Ryan et al., 2014b). This combination of a multi-detector array and an ultra-bright collimated source enables a combination of high spatial resolution (~2 microns), sensitivity to concentrations in the hundreds to low thousands of ppm range and rapid data collection, such that cm^2 areas can be scanned in a matter of a few hours. Numerous studies have revealed a range of types of trace element distributions, not only in igneous minerals but also in a wide range of other geological and non-geological applications (Cleverley et al., 2012; Dyl et al., 2014; Ryan et al., 2014b; Fisher et al., 2015; Barnes et al., 2016b; Holwell et al., 2016).

Igneous pyroxenes are especially informative recorders of magmatic histories, in that they crystallise over a wide range of conditions and incorporate a range of elements with different geochemical characteristics into their crystal structure (Putirka, 2017). Trace elements in individual pyroxene grains have been mapped by laser ablation – ICPMS in recent studies (Ubide et al., 2015, 2019; Ubide and Kamber, 2018), showing the presence of sector zoning in Ti and oscillatory zoning in Cr in the same grain. These elements appear to be particularly susceptible to zoning on account of their relatively slow diffusion rates compared with divalent transition metals such as Ni and Mn (Cherniak et al., 2010).

Trace element zoning in pyroxenes associated with magmatic sulfide ore deposits in ultramafic-mafic intrusions has been investigated using Maia detector based XFM at the Australian Synchrotron (Barnes et al., 2016b; Mao et al., 2019). As in the Mt Etna studies (Ubide et al., 2015, 2019; Ubide and Kamber, 2018), the usually non-divalent elements Cr and Ti appear to be the most informative. Their non-divalent character results in slow diffusion rates, as it is necessary to break Si-Al bonds in the host pyroxene structure to accommodate charge balance. This property allows subtle zoning to be retained even in slowly-cooled intrusions emplaced in the mid-crust (Taranovic et al., 2019). However, even with the benefits of the Maia-XFM method, effective detection limits restrict the usefulness of the method to either products of relatively primitive magmas, to generate sufficiently high Cr contents in pyroxenes, or products of evolved magmas where Ti contents are higher but Cr contents are generally too low to be detectable, using the conventional mapping technique with beam energies high enough to excite all of the first row transition elements.

In this contribution, we report results of a modified synchrotron XFM approach involving input energies just below the Fe K absorption edge. By eliminating the very high-yield Fe Kα X-rays, this modification allows greatly enhanced sensitivity for elements lighter than Fe, particularly Cr and Ti.

We show examples of the benefits of this technique applied to samples of Mt Etna trachybasalts and pyroxene-bearing dolerites from the Norilsk region in Siberia. In both cases the additional sensitivity of the technique reveals details at spatial scales not previously attainable even with synchrotron radiation using the conventional approach.

Samples

Sample 15RC017 is a basaltic bomb from the 1974 flank eruption at Mt Etna (Sicily, Italy). The 1974 flank eruption is an archetypical example of 'eccentric' or 'deep-dyke-fed' eruption, tapping deep, pre-degassed magma through pathways that bypass the central conduits of the volcano (Corsaro et al., 2009; Ubide and Kamber, 2018). The bomb belongs to the second phase of the eruption (11-29 March 1974; Corsaro et al., 2009 and references therein) and was sampled at the base of the Mount De Fiore II scoria cone, at UTM 33S 493347 4177339. The sample is a mildly vesicular and microporphyritic trachybasalt, with <5 vol.% microphenocrysts of clinopyroxene that are commonly sector-zoned and associated into glomerocrysts. Clinopyroxene typically occurs together with titanomagnetite and less commonly with olivine. The rock groundmass is dominated by plagioclase microlites and glass. The sample was previously investigated as part of clinopyroxene studies focused on the interpretation of magmatic processes recorded in oscillatory zoning (Ubide and Kamber, 2018) and sector zoning (Ubide et al., 2019).

Sample 24-93.6 comes from the Norilsk 1 intrusion, an ore-bearing high-level subvolcanic sill forming part of the Siberian Large Igneous Province (Ryabov et al., 2014; Sluzhenikin et al., 2014). The sample, from a drill hole close to the Medvezhy Creek open pit Ni-Cu-PGE mine, at UTM 45W 546400 7686100, is a Cr-spinel rich olivine dolerite from the upper zone of the intrusion. The zone is characterised by low-S, high-PGE mineralisation, highly heterogeneous textures with abundant sedimentary xenoliths and irregular oxide-rich clots a few mm in size consisting of clusters of Cr-magnetite and chromite, amygdales and widely dispersed platinum group element minerals (Ryabov et al., 1982; Ryabov et al., 2014). Clinopyroxene occurs as a poikilitic to interstitial phase in the gabbroic matrix, and growing inward from the walls of segregation vesicles (Barnes et al., 2019) associated with the spinel-rich clots.

Method

Maia-XFM data were collected at the XFM beamline of the Australian Synchrotron using the Kirkpatrick Baez mirror microprobe end-station. This provides a monochromatic 2 µm beam spot size for energies in the range 4–20 keV. Equipped with the Maia 384 detector array, the XFM beamline can acquire data at 2 µm resolution from 384 detectors simultaneously over areas of several square centimetres with count rates of 4–10 M/s, and energy resolution of around 260 eV (Kirkham et al., 2010; Ryan et al., 2010; Paterson et al., 2011; Ryan et al., 2014b). Data are acquired in event mode

(Ryan et al. 2014b) with each detected X-ray event tagged by detector number in the array and X, Y scan pixel coordinate in records tagged by accumulated flux and transit time per pixel. The data are analyzed, event by event, using the Dynamic Analysis (DA) method for real-time spectral deconvolution, which accumulates element concentration maps with the effects of spectral overlap, pileup and background removed (Ryan 2010). The DA method uses a standardless approach based on a fundamental parameter model (Kirkham et al., 2010; Ryan et al., 2010; Paterson et al., 2011; Ryan et al., 2014b) implemented in the GeoPIXE software package. Maps were collected using incident beam energies of 7.05 and 18.5 KeV for the low- and high-energy scans respectively, at spatial resolution of 2 μm and a scanning velocity of 5 mm/s, giving an effective dwell time of 0.4 ms per pixel. Yield corrections were calculated from a major element composition of clinopyroxene obtained by electron microprobe analysis using the Jeol instrument at CSIRO Mineral Resources, Clayton. Minor element data from microprobe analyses were also determined for comparison.

Results

Mt Etna sample

A composite RGB map of the Etnean trachybasalt (Red-Cr, Green-Ti, Blue-Ca; Figure 1A-D) highlights the mineral assemblage composed of micro-phenocrysts of clinopyroxene (light blue, high Ca-Ti), olivine (red, low Ca-Ti), magnetite (yellow, high Ti-Cr), and microlites of plagioclase (blue, moderate Ca) embedded in a glassy groundmass. The internal zonation of clinopyroxene crystals is particularly complex and interesting. Many of the clinopyroxenes show concentric enrichments in Cr associated with depletion in Ti. These zones were previously shown to be enriched in Mg and transition metals and depleted in incompatible elements, reflecting growth after new injections of mafic melt into the crystallising reservoir (Ubide and Kamber, 2018). The XFM map presented here allows a rapid statistical evaluation on the occurrence of Cr-rich zones. It is also evident from Fig. 1A that complex zoning is a consistent feature of all pyroxene phenocrysts in the sample, with the nature of the pattern depending on the crystallographic orientation relative to the section plane. Cr-rich zones often overgrow previous cores, but also commonly occur in the centre of grains marking the position of original nucleii formed upon magma recharge. In addition, the map reveals the frequent occurrence of sector zoning in the clinopyroxene crystals, clearly distinguished by the relative abundance of Ti in prism sectors (high Ti) relative to hourglass sectors (low Ti; Figure 1D, 1F). As shown in Ubide et al. (2019), the striking decoupling of minor and trace elements into sectors vs. concentric zones is related to the ionic potential of each cation (cation charge relative to the squared radius of the crystallographic site it occupies in the clinopyroxene lattice) which, in turn, controls the efficiency of the cation in charge balance mechanisms. This explains why titanium (Ti^{4+}) is strongly sector zoned, whereas chromium (Cr^{3+}), which also partitions into the M1 site, is preliminarily distributed along concentric growth zones (Figure 1D-F). Sector and/or oscillatory zoning are observed in most

clinopyroxene crystals, reflecting conditions of magma undercooling and mafic recharge, respectively (Ubide et al., 2019).

Figure 1 Etna sample 15RC017 maps.

Norilsk sample

Clinopyroxenes in the gabbroic rocks of the Norilsk-Talnakh intrusions record the crystallisation of the liquid component of the sills, which in most cases represents the trapped intercumulus liquid interstitial to cumulus silicates and oxides. In the example studied here, the clinopyroxene grows from the liquid "matrix" to an assemblage of Cr-spinel clusters or small rafts, along with minor amounts of locally skeletal olivine. The sample mapped in Fig. 2 is representative of the unusual PGE-rich, sulfide poor upper taxitic zone of the Norilsk 1 intrusion, and is characterised by the presence of cm-scale clumps or mats of Cr-spinel and Cr-magnetite with distinctive cuspate morphologies, interpreted as the result of the former presence of gas bubbles (Barnes et al., 2019; Le Vaillant et al., 2017). The spinel clumps appear to be selectively attached to bubble walls, probably because of physical collection of spinel grains by rising bubbles within the upper part of the sill, analogous to a model previously proposed for podiform chromitites (Matveev and Ballhaus, 2002) or due to selective nucleation of bubbles within spinel mats owing to surface tension effects (Plese et al., 2019). The silicate matrix to the clumps is a heterogenous gabbro, with typical ophitic texture and a common occurrence of zoned clinopyroxenes growing away from the cluster walls (Figure 2B-E) and also in many cases (Figure 2F) growing inward from the walls of what are now segregation vesicles, i.e. former voids now occupied by inward-leaking silicate melt (Barnes et al., 2019). Clinopyroxenes, as typical throughout the intrusion, are characteristically normally zoned with respect to Cr, reflecting the high compatibility of Cr^{3+} in clinopyroxene and the consequent progressive depletion in the residual liquid component as clinopyroxene crystallises. Based on currently available data from high-energy synchrotron XFM mapping (Barnes et al., 2019) this zonation is usually regular, concentric and monotonic. However, the new data collected at low incident beam energy reveal a more complex pattern of oscillatory zoning with a sharp boundary to a low Cr rim, coupled with a sharp internal interface in the upper right corner of the grain defined by both Cr and Ti, probably reflecting sector-zoning (Figure 2). Evidently the partitioning of Cr into the pyroxene was either limited by diffusion, or was modified by fluctuating external conditions such as volatile release. An external control would result in correlatable patterns of zoning among different grains in the same sample, testable by more extensive mapping of multiple grains on thin section scale.

Figure 2 Sample 24-39.3B from Upper Taxite of Norilsk 1 intrusion.

Comparison of low and high energy scans

The contrast between the quality of the X-ray spectra collected at low and high energy is shown in Figure 3; aside from the change in elastic and inelastic scatter energies associated with the beam,

differences are evident largely in a thirty-fold improvement in signal (and hence sensitivity) at low energy for Ti and Cr.

Figure 3 Comparison of spectra

The improvement in precision is especially evident in comparing measured concentrations along a line traverse through the oscillatory zoned pyroxene in the Norilsk sample (Figure 4). The analytical precision is improved by an order of magnitude in the low-Energy scan. The subtle intermediate peak visible in the low-Energy scan is lost in the noise in the high-Energy scan.

Figure 4. Comparison of linear traverses

Implications

These results demonstrate that the resolution of subtle minor element zoning in igneous samples, particularly in Ti and Cr, is greatly enhanced in synchrotron XFM images by scanning below the Fe K edge. In the examples shown here, the zoning patterns reveal aspects of the crystallisation history that are not evident from conventional XFM images.

The advantages of Maia-XFM mapping over other techniques are largely related to the high spatial resolution (2 μm) coupled with analytical precision at 100 ppm levels at short dwell times, particularly for transition metals. Laser ablation – ICPMS mapping has higher sensitivity to more elements at lower detection limits (down to sub-ppm), but the spatial resolution is typically poorer, of the order of tens of μm, and only a small number of grains can be analysed in a reasonable time with regular quadrupole MS set-ups (e.g., Ubide et al., 2015, 2019a, 2019b). The individual grain LA-ICPMS images in Fig. 1 E and F took an hour and ten minutes to collect, compared with two hours for the roughly twenty times larger area in XFM image B. The Maia-XFM method allows entire thin sections to be imaged in a matter of hours, identifying particular grains of interest that can then be followed up by other geochemical methods, if required. However, the information obtained directly from the XFM maps is sufficient in itself to reveal magmatic histories. One particular advantage is that the method can generate quantitative diffusion profiles across every compositional boundary in the image, enabling true-width profiles to be identified by finding the steepest concentration gradients representing sections orthogonal to the grain boundary. We recommend this approach for reading magmatic processes from crystal cargoes in a wide variety of volcanic and intrusive settings, with applications to determination of crystal residence times and potentially to the assessment of prospectivity of mafic intrusions for magmatic ore deposits.

Acknowledgments

We thank Marina Yudovskaya for providing the Norilsk sample and Brianna Ganley and Anaïs Pagès for helpful reviews of an early draft. Zoja Vukmanovic and an anonymous reviewer are thanked for

constructive reviews. This research was undertaken on the X-ray Fluorescence Microscopy beamline at the Australian Synchrotron, part of ANSTO.

References

Barnes, S.J., Fisher, L.A., Godel, B., Maier, W.D., Paterson, D., Howard, D.L., Ryan, C.G., and Laird, J.S. (2016a) Primary cumulus platinum minerals in the Monts de Cristal Complex, Gabon: magmatic microenvironments inferred from high-resolution x-ray fluorescence microscopy Contributions to Mineralogy and Petrology, 171, 23.

Barnes, S.J., Le Vaillant, M., Godel, B., and Lesher, C.M. (2019) Droplets and bubbles: solidification of sulphide-rich vapour-saturated orthocumulates in the Noril'sk-Talnakh Ni-Cu-PGE ore-bearing intrusions Journal of Petrology, 60, 269-300.

Barnes, S.J., Mole, D.R., Le Vaillant, M., Campbell, M., Verrall, M., Roberts, M., and Evans, N.J. (2016b) Poikilitic textures, heteradcumulates and zoned orthopyroxenes in the Ntaka Ultramafic Complex, Tanzania: implications for crystallisation mechanisms of oikocrysts. Journal of Petrology, 57, 1171-1198.

Barnes, S.J., Pina, R., and Le Vaillant, M. (2018) Textural development in sulfide-matrix ore breccias in the Aguablanca Ni-Cu deposit, Spain, revealed by X-ray fluorescence microscopy. Ore Geology Reviews, 95, 849-862.

Cherniak, D.J., Dimanov, A., Zhang, Y., and Cherniak, D. (2010) Diffusion in pyroxene, mica and amphibole. Reviews in Mineralogy and Geochemistry, 72, 641-690.

Cleverley, J.S., Ryan, C.G., Hough, R.M., Bland, P.A., Fisher, L.A., Dyl, K.A., and Anonymous. (2012) Quantified, whole section, MAIA XRF mapping of trace elements in Allende. Meteoritics & Planetary Science, 47, Suppl., Abstract no. 5175.

Corsaro, R.A., Métrich, N., Allard, P., Andronico, D., Miraglia, L., and Fourmentrau, x.C. (2009) The 1974 flank eruption of Mount Etna: an archetype for deep dike-fed eruptions at basaltic volcanoes and a milestone in Etna's recent history. Journal of Geophysical Research, 114, B07204.

Costa, F., and Morgan, D. (2011) Time constraints from chemical equilibration in magmatic crystals. In A. Dossetto, S.P. Turner, and J.A. Van Orman, Eds. Timescales of Magmatic Processes: from Cire to Atmosphere. Blackwell, Chichester.

Dyl, K.A., Cleverley, J.S., Bland, P.A., Ryan, C.G., Fisher, L.A., and Hough, R.M. (2014) Quantified, whole section trace element mapping of carbonaceous chondrites by synchrotron X-ray fluorescence microscopy; 1, CV meteorites. Geochimica et Cosmochimica Acta, 134, 100-119.

Fisher, L.A., Fougerouse, D., Halfpenny, A., Ryan, C.G., Micklethwaite, S., Hough, R.M., Cleverley, J.S., Gee, M., Paterson, D., and Howard, D. (2015) Fully quantified, multi-scale element mapping of mineral system samples using the Maia detector array: recognizing chemical variation on micron to cm scales. Mineralium Deposita, 50, 665-674.

Holwell, D.A., Barnes, S.J., Le Vaillant, M., Keays, R.R., Fisher, L., and Prosser, R. (2016) 3D textural evidence for the formation of ultra-high tenor precious metal bearing sulfide microdroplets in offset reefs: an extreme example from the Platinova Reef, Skaergaard Intrusion, Greenland. Lithos, 256, 55-74.

Kirkham, R., Dunn, P., Kuczewski, A., Siddons, D., Dodanwela, R., Moorhead, G., Ryan, C., De Geronimo, G., Beuttenmuller, R., Pinelli, D., Pfeffer, M., Davey, P., Jensen, M., Paterson, D., de Jonge, M., Kusel, M., and McKinlay, J. (2010) The Maia spectroscopy detector system: engineering for integrated pulse capture, low-latency scanning and real-time processing. Proceedings of Australian Institute of Physics 1234, 240-243.

Le Vaillant, M., Barnes, S.J., Mungall, J.E., Mungall, E., 2017. Role of de-gassing of the Noril'sk nickel deposits in the Permo-Triassic mass extinction event. Proceedings of the National Academy Of Sciences 114, 2485-2490

Lynn, K.J., Shea, T., Garcia, M.O., Costa, F., and Norman, M.D. (2018) Lithium diffusion in olivine records magmatic priming of explosive basaltic eruptions. Earth and Planetary Science Letters, 500, 127-135.

Mao, Y.-J., Barnes, S.J., Qin, K.Z., Tang, D.M., Martin, L., Su, B.X., and Evans, N.J. (2019) Sector zoned orthopyroxene, olivine oxygen isotope and trace elemental stratigraphic variations in the Huangshanxi orthopyroxene-rich Ni-Cu deposit, northwest China: implications for rapid orthopyroxene growth induced by silica assimilation. Contribution to Mineralogy and Petrology, 174, 33.

Matveev, S., and Ballhaus, C. (2002) Role of water in the origin of podiform chromitite deposits. Earth and Planetary Science Letters, 203, 235- 243.

Mollo, S., Blundy, J.D., Iezzi, G., Scarlato, P., and Langone, A. (2013) The partitioning of trace elements between clinopyroxene and trachybasaltic melt during rapid cooling and crystal growth. Contributions to Mineralogy and Petrology, 166(6), 1633-1654.

Paterson, D., de Jonge, M.D., Howard, D.L., Lewis, W., McKinlay, J., Starritt, A., Kusel, M., Ryan, C.G., Kirkham, R., Moorhead, G., and Siddons, D.P. (2011) The X-ray Fluorescence Microscopy Beamline at the Australian Synchrotron. Proceedings of the Australian Institute of Physics, 1365, 219-222.

Plese, P., Higgins, M.D., Baker, D.R., Lanzafame, G., Prasek, M.K., Mancini, L., and Rooyakkers, S.M. (2019) Production and detachment of oxide crystal shells on bubble walls during experimental vesiculation of andesitic magmas. Contributions to Mineralogy and Petrolog, 174:21.

Putirka, K.D. (2017) Down the Crater: Where Magmas are Stored and Why They Erupt. Elements, 13(1), 11-16.

Ryabov, V.V., G., T.V., and Ya., Y.I. (1982) Concentration of chromium and platinum-group elements in the roofs of Noril'sk-type layered intrusions. Doklady Akadamia Nauk SSSR, 226, 466-469.

Ryabov, V.V., Shevko, A.Y., and Gora, M.P. (2014) Trap Magmatism and Ore Formation in the Siberian Noril'sk Region. 625 p. Springer, Dordrecht.

Ryan, C.G., Kirkham, R., Hough, R.M., Moorhead, G., Siddons, D.P., de Jonge, M.D., Paterson, D.J., De Geronimo, G., Howard, D.L., and Cleverley, J.S. (2010) Elemental X-ray imaging using the Maia detector array: The benefits and challenges of large solid-angle. Nuclear Instruments & Methods in Physics Research Section A - Accelerators Spectrometers Detectors and Associated Equipment, 619, 37-43.

Ryan, C.G., Siddons, D.P., Kirkham, R., Li, Z.Y., de Jonge, M.D., Paterson, D.J., Cleverley, J.S., Kuczewski, A., Dunn, P.A., Jensen, M., De Geronimo, G., Howard, D.L., Godel, B., Dyl, K.A., Fisher, L.A., Hough, R.M., Barnes, S.J., Bland, P.A., Moorhead, G.F., James, S.A., Spiers, K.M., Falkenberg, G., U , Boesenberg, U., and Wellenreuther, G. (2014a) The Maia detector array and x-ray fluorescence imaging system: locating rare precious metal phases in complex samples Proc. SPIE 8851, X-Ray Nanoimaging: Instruments and Methods, 8851, 88510Q.

Ryan, C.G., Siddons, D.P., Kirkham, R., Li, Z.Y., de Jonge, M.D., Paterson, D.J., Kuczewski, A., Howard, D.L., Dunn, P.A., Falkenberg, G., U , Boesenberg, U., De Geronimo, G., Fisher, L.A., Halfpenny, A., Lintern, M.J., Lombi, E., Dyl, K.A., Jensen, M., Moorhead, G.F., Cleverley, J.S., Hough, R.M., Godel, B., Barnes, S.J., James, S.A., Spiers, K.M., Alfeld, M., Wellenreuther, G., Vukmanovic, Z., and Borg, S. (2014b) Maia X-ray fluorescence imaging: Capturing detail in complex natural samples. Journal of Physics: Conference Series, 499, 012002.

Seitz, S., Putlitz, B., Baumgartner, L., Meibom, A., Escrig, S., and Bouvier, A.-S. (2018) A NanoSIMS Investigation on Timescales Recorded in Volcanic Quartz From the Silicic Chon Aike Province (Patagonia). Frontiers in Earth Science, 6(95).

Sluzhenikin, S.F., Krivolutskaya, N.A., Rad'ko, V., Malitch, K.N., Distler, V.V., and Fedorenko, V.A. (2014) Ultramafic-mafic intrusions, volcanic rocks and PGE-Cu-Ni sulfide deposits of the Noril'sk Province, Polar Siberia, Field Trip Guidebook. Institute of Geology of Ore Deposits, Petrography, Mineralogy and Geochemistry., Yekaterinburg, Russia.

Taranovic, V., Barnes, S.J., and Beresford, S.W. (2019) Nova – Bollinger Ni – sulfide Ore Deposit, Albany-Fraser Orogen, Western Australia: Petrology, Geometry and Emplacement of the Host Intrusions. SGA. SGA, Glasgow.

Ubide, T., and Kamber, B.S. (2018) Volcanic crystals as time capsules of eruption history. Nature Communciations, 9, 326.

Ubide, T., McKenna, C.A., Chew, D.M., and Kamber, B.S. (2015) High-resolution LA-ICP-MS trace element mapping of igneous minerals; in search of magma histories. Chemical Geology, 409, 157-168.

Ubide, T., Mollo, S., Zhao, J.X., Nazzari, M., and Scarlato, P. (2019) Sector-zoned clinopyroxene as a recorder of magma history, eruption triggers, and ascent rates. Geochimica et Cosmochimica Acta., 251, 265-283.

Ubide, T., Caulfield, J., Brandt, C., Bussweiler, Y., Mollo, S., Di Stefano, F., Nazzari, M. and Scarlato, P. (2019b). Deep magma storage revealed by multi-method elemental mapping of clinopyroxene megacrysts at Stromboli volcano. Frontiers in Earth Science, DOI: 10.3389/feart.2019.00239.

Wang K.-Y., Song X.Y., Yi J.-N., Barnes S.J., She Y.-W., Zheng Q.-Q., Schoneveld L.E., 2019, Zoned orthopyroxenes in the Ni-Co sulfide ore-bearing Xiarihamu mafic-ultramafic intrusion in northern Tibetan Plateau, China: Implications for multiple magma replenishments. Ore Geology Reviews, online: doi: 10.1016/j.oregeorev.2019.103082.

Welsch, B., Faure, F., Famin, V., Baronnet, A., and Bachelery, P. (2013) Dendritic crystallization; a single process for all the textures of olivine in basalts? Journal of Petrology, 54(3), 539-574.

Figure captions

Figure 1: Mapping of Etna sample 15RC017. A, B, Maia XFM images collected at 7050 eV (A) and 18500 eV incident beam energy (B). Image size 15000 x 5764 pixels, acquisition time was 2 h. C,D, enlargement of selected pyroxene grains showing concentric zonation in Cr and sector zoning in Ti. E,F, laser ablation – ICPMS element maps of pyroxene D (acquisition time was 1 h and 10 min). Colour scales indicate concentrations in ppm (Cr up to 1000 ppm, Ti to 10,000 ppm) in clinopyroxene; concentrations in other phases occurring as inclusions or in the groundmass are semi-quantitative.

Figure 2: Sample 24-39.3B from Upper Taxite of Norilsk 1 intrusion. A) high-energy scan (18500 eV) of domain showing a large cluster of Cr-spinel with smooth concave margins interpreted as original vapour bubble walls, now infilled by mix of plagioclase-pyroxene (right) and amygdale-filling chlorite and other fine grained phases (lower left). Note ingrowth of Cr-Ti zoned clinopyroxene from original bubble wall (centre) (sqr indicates square root of count rate). B, low-energy scan (7050 eV) showing details of complexly zoned clinopyroxene with rim of relatively Ti-enriched replacive amphibole, and fine radiating acicular Mn-bearing phase (green) in amygdale (left). C, same area, scanned at high energy (18500 eV); no lack of detail compared with low-E scan. D,E, low energy scan (7050 eV) of same area, single-element concentration maps of Cr and Ti. Image size 1750 x 1426 pixels, acquisition time 10 mins. F, different area from same sample showing clinopyroxene growing into a segregation vesicle from inner wall of thin Cr-magnetite bubble rind (Cr abundance in

shades of yellow (combined red and green), Ti blue, showing combination of sector and oscillatory zoning.

Figure 3 Comparison of spectra from low and high energy scans of the Etna sample (integrated over area indicated by white dashed line). Red = smoothed spectrum, green = raw data, purple = best fit background.

Figure 4. Comparison of quantified Cr concentration along linear traverse from core to rim of zoned clinopyroxene in Norilsk sample (Fig. 2) for low and high energy scans – average plus 2-sigma error bars. White-line profile on lower plot is Cr data from electron microprobe along a closely adjacent traverse.

Supplementary material:

Fig Supp1 – Maia-XFM map of Etna sample 15RC017, low incident energy, Cr (red) – Ti (green) – Ca (blue) RGB image at full resolution (corresponding to Fig 1A).

Fig Supp2. Maia-XFM map of Etna sample 15RC017, low incident energy, Cr concentration map, square root scale, full resolution (corresponding to detailed area in Fig 1, D,E,F).

Fig Supp3. Maia-XFM map of Etna sample 15RC017, low incident energy, Ti concentration map, log scale, full resolution (corresponding to detailed area in Fig 1, D,E,F).

This is a preprint, the final version is subject to change, of the American Mineralogist (MSA)
Cite as Authors (Year) Title. American Mineralogist, in press.
DOI: https://doi.org/10.2138/am-2020-7228

Figure 1

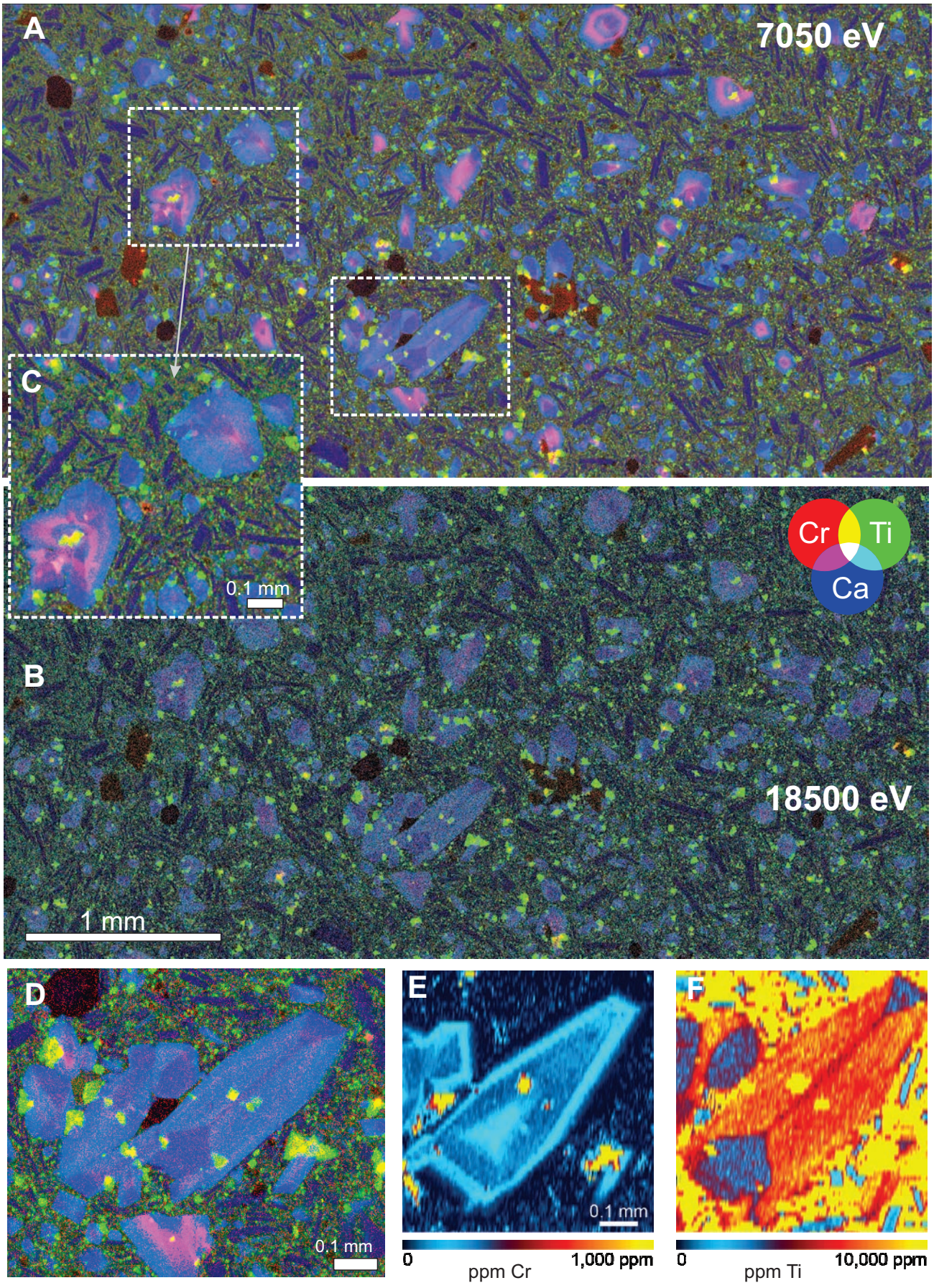

This is a preprint, the final version is subject to change, of the American Mineralogist (MSA)
Cite as Authors (Year) Title. American Mineralogist, in press.
DOI: https://doi.org/10.2138/am-2020-7228

Figure 2

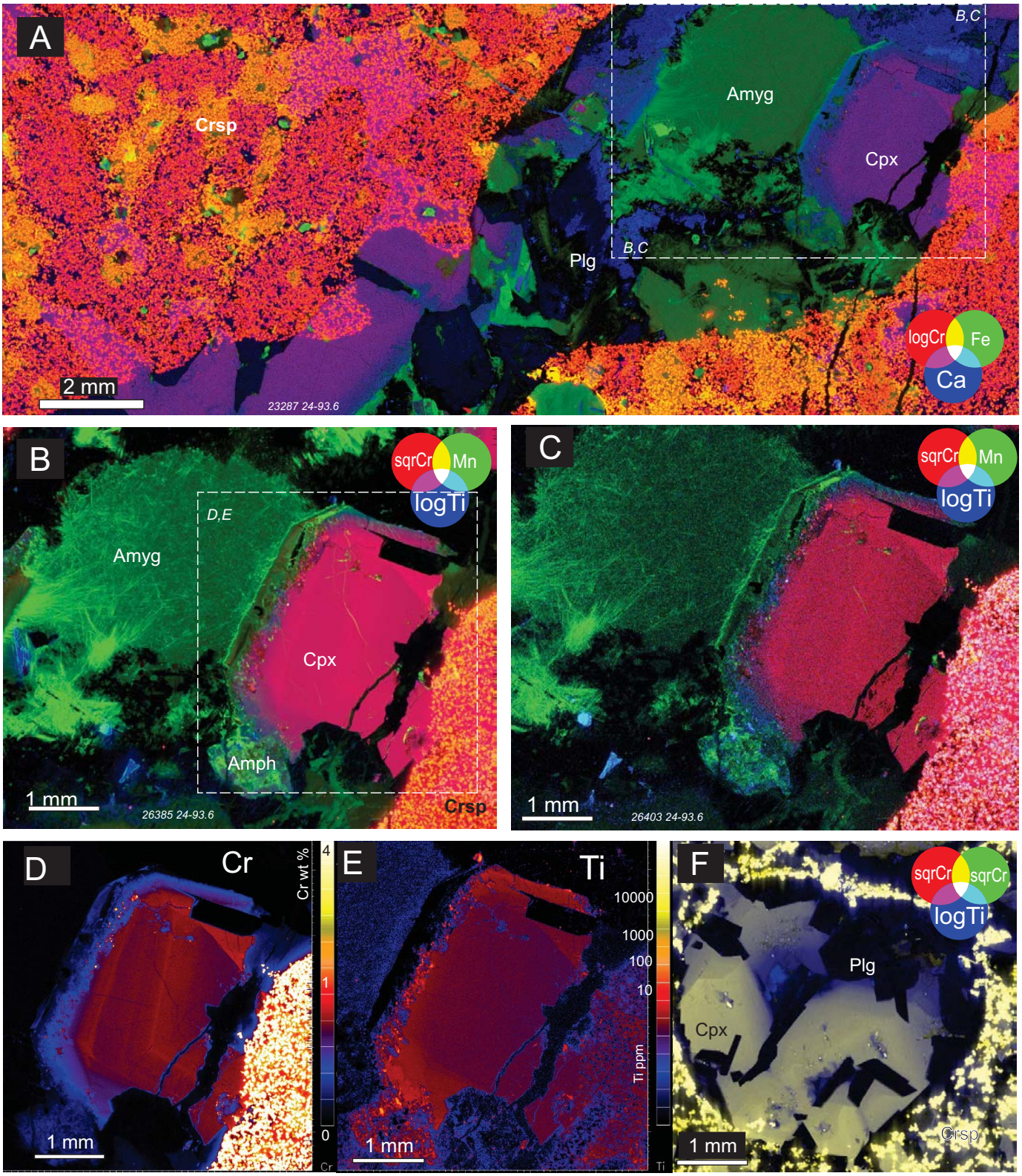

This is a preprint, the final version is subject to change, of the American Mineralogist (MSA)
Cite as Authors (Year) Title. American Mineralogist, in press.
DOI: https://doi.org/10.2138/am-2020-7228

Figure 3

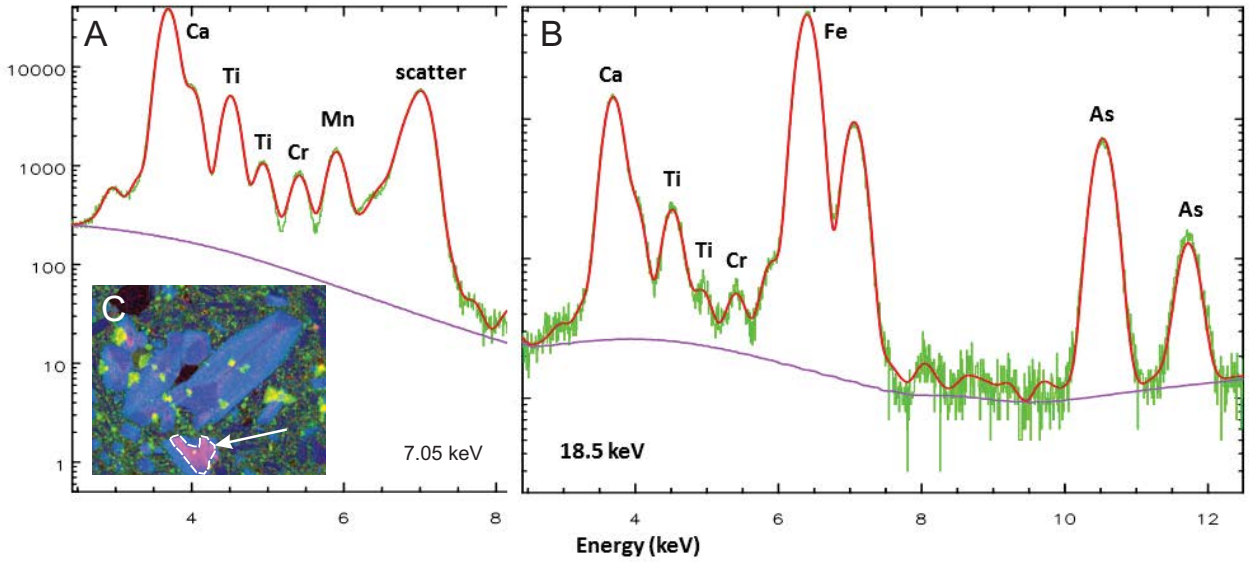

This is a preprint, the final version is subject to change, of the American Mineralogist (MSA)
Cite as Authors (Year) Title. American Mineralogist, in press.
DOI: https://doi.org/10.2138/am-2020-7228

Figure 4